ORNL/SPR-2023/2939

Impact of LWR Assembly Structural Features on Cladding Burst Behavior under LOCA Conditions

D. Schappel
N. Capps

July 2023

OAK RIDGE National Laboratory

ORNL IS MANAGED BY UT-BATTELLE LLC FOR THE US DEPARTMENT OF ENERGY

ORNL/SPR-2023/2939

Nuclear Energy and Fuel Cycle Division

IMPACT OF LWR ASSEMBLY STRUCTURAL FEATURES ON CLADDING BURST BEHAVIOR UNDER LOCA CONDITIONS

D. Schappel
N. Capps

July 2023

Prepared by
OAK RIDGE NATIONAL LABORATORY
Oak Ridge, TN 37831
managed by
UT-BATTELLE LLC
for the
US DEPARTMENT OF ENERGY
under contract DE-AC05-00OR22725

CONTENTS

LIST OF FIGURES

LIST OF TABLES

ABBREVIATIONS

2D RZ	Two dimensions, radial and height
3D	three dimensions, Cartesian coordinates
BDBA	beyond design basis accident
FFRD	fuel fragmentation relocation and dispersal
INL	Idaho national laboratory
LB LOCA	large break loss of coolant accident
LOCA	loss of coolant accident
NFIR	nuclear fuel industry research
NRC	U.S. Nuclear Regulatory Commission
PWR	pressurized water reactor
RIL	Research Information Letter
TCR	Transformational Challenge Reactor

ABSTRACT

The previous work focused on core optimization via neutronics, thermal hydraulics and thermos-mechanical analysis for burnups beyond 62 GWD/tU and enrichments above 5%. Also investigated was uncertainty of fuel fragmentation relocation and dispersal in high burnup rods during accident conditions. The dispersal aspect of fuel fragmentation depends on cladding rupture. Thus, assessing uncertainties in the rupture behavior is helpful to estimating the dispersal of high burnup fuel.

This report builds on the previous work by assessing the impact of assembly structural features on cladding balloon and burst behavior in a full-length fuel rod. In this work, the BISON fuel performance code was used to generate 2D RZ meshes containing structural features commonly used in nuclear fuel assemblies. Firstly, meshes were generated with spacer grids. Then results were then compared to the cladding burst temperature and balloon strain results from the previous work. A mesh sensitivity study was performed to ensure mixing veins and spacer grid effects were appropriately considered, resulting in a more refined mesh than the previous study. The balloon deformation and burst times of the cladding were compared to the original case. Consideration was also given to the effect of rod initial pressure. Overall, the BISON simulations indicated that the assembly structural features can locally influence cladding performance; however, the impact on the overall cladding performance was minor during a loss-of-coolant accident.

1. INTRODUCTION

The US nuclear fleet community is continuing to develop a technical basis to support burnup extension and, more specifically, to address the safety implications of high-burnup fuel fragmentation, relocation, and dispersal (FFRD) under a loss-of-coolant accident (LOCA) condition. Two approaches have been considered to date. The first is a deterministic and risk-informed approach intended to justify the classification of a large break LOCA (LB LOCA) as a beyond design basis accident (BDBA) and thus not requiring further consequence analysis to satisfy 10 CFR 50.46 [1]. The justification is predicated on the use of a leak-before-break analysis methodology, which has been used to determined that a double-guillotine break has an extremely low probability of rupture, and, therefore, a risk-informed approached, as outlined in Regulatory Guide 1.174 [2], could be used to assess whether FFRD must be considered in standard deterministic LOCA analysis methodologies [3]. The probability of these events depend on the size of LOCA, but vary from about 10^{-4} to 10^{-9} [4].

The second approach intends to use a best estimate plus uncertainty approach to quantify cladding rupture and dispersal susceptibility [2, 5, 6, 7]. From there, the licensees can determine whether additional analyses (criticality, dispersed particle coolability, source term, etc.) must be performed to address safety subsequent concerns. Additionally, this approach supports the use of a no-burst criteria (i.e., cladding burst) and could be leveraged by the first approach to strengthen defense in depth. In the event of clad burst, there is the possibility of flow obstruction and local of coolability for that channel. Thus, designing the reactor to avoid clad burst and providing mechanisms for mitigating the consequences of the burst increases the defense in depth of the reactor. The approach outlined in the literature [2, 5, 6, 7] made a number of assumptions to ultimately calculate dispersal susceptibility that may increase or reduce the amount of fuel susceptible to dispersal. Of these assumptions, the cladding balloon behavior, transient fission gas release on cladding performance, and the impact of assembly structural features are particularly important to consider.

The U.S. Nuclear Regulatory Commission (NRC) published a Research Information Letter (RIL 2021-13) [8] that used experimental data to describe five elements of FFRD. Two of the elements deal specifically with the balloon geometry and rupture timing. The first of the two suggests a cladding strain threshold exists, in which fragmented fuel will be prevented from relocating and being susceptible to dispersal. The second element intends to address concerns of pre-mature rupture by transient fission gas release. Previous work [2, 4, 5, 6] assumed that assembly structural features would limit FFRD to the grid zone in which the rupture occurred. However, the assembly structural features were not explicitly modeled, and, as a result, the cladding balloon across most of the rod exceeded the cladding strain threshold documented in the RIL. The purpose of this work is to investigate the impact of assembly structural features to clarify this assumption and corresponding uncertainties. Assembly structural features along with the cladding fuel rod were modeled in BISON during the steady state and LOCA transient. The behavior of the cladding was closely monitored during all periods of the simulation and compared to a simulation for which the structural features were not considered. During the transient, cladding strain (i.e., balloon geometry) was evaluated along with the burst conditions. The results were used to validate or correct assumptions made in the previous work.

2. MATERIAL CORRELATIONS

The material models used in this work are described in detail in the BISON repository maintained by Idaho National Laboratory (INL) [9]. A brief description of the material properties is given below.

2.1 UO_2

The Nuclear Fuel Industry Research (NFIR) [10] thermal conductivity model without gadolinium was used for UO_2. The specific heat is from Luscher et al. [11]. The elastic modulus and Poisson's ratio [12] were set to 200 GPa and 0.345, respectively, per BISON default settings.

The creep model is from Allison et al. [13]. The coefficient of thermal expansion was set to a constant 10^{-6} (-) as per the BISON default setting. The volumetric change was divided into densification [14], solid fission product swelling, and gaseous fission product swelling [13].

2.2 ZIRCALOY

The zircaloy thermal conductivity is given by Allison et al. [13]. The specific heat is also based on data from Allison et al. [13]. The model uses linear interpolation between data points with values of about 300–800 J/kg·K. The trend is about 300–350 J/kg·K until 1100 K, at which point it rapidly increases to about 800 J/kg·K at 1170 K, then returns to approximately 350 J/kg·K at 1250 K.

The elastic properties were calculated with the MATPRO correlations [15], which are a function of temperature. The Erbacher [16] model was selected for the thermal creep. Irradiation creep was included in the simulations. Plasticity was not included in the final simulations. It was possible to include plasticity in the 2D simulations however the 3D simulations would not converge with plasticity. For consistency plasticity was removed from all simulations. However, the clad bursting occurred during the LOCA, where thermal creep dominated the clad deformation. Table 1 lists the material properties used in this work.

Table 1. List of material properties used in this work.

	UO_2	**Zircaloy**
Thermal conductivity	Marion (NFIR) [10]	Allison et al. [13]
Specific heat	Luscher et al. [11]	Allison et al. [13]
Thermal expansion	BISON default	RELAP5 [15]
Creep	Allison et al. [13]	Erbacher [16]
Swelling	Rashid et al. [14] and Allison et al. [13]	Luscher et al. [17] and [14]
Elastic modulus	BISON default	MATPRO [15]
Poisson's ratio	BISON default	MATPRO [15]
Rupture	NA	Blacker et al. [18] and Marcello et al. [19]

3. METHODS

The BISON fuel performance code [20, 21], developed by INL, was used to perform the simulations presented in this work. BISON is finite element code built upon the MOOSE [22, 23, 24] enabling rapid model development and simulation of complex 1D, 2D, and 3D geometries. The mesh geometries were developed in Cubit [18], developed by Sandia National Laboratory, and exported to BISON.

This work leverages the 2D RZ fuel rod symmetry. It should be noted that fuel rods in a reactor will likely have asymmetric heating profiles resulting in potential asymmetric ballooning behavior. However, capturing the asymmetric temperature conditions experienced by the fuel rod would require 3D thermal

hydraulic boundary conditions. Another consideration is the fuel rod and assembly features geometry. The fuel rod and structural features are listed in

Table 2, and an image of the features are shown below in Figure 1. Due to the aspect ratio of the fuel rod, Figure 1 simply shows small sections of the fuel rod containing the plenum, base, and a spacer grid.

Table 2. List of fuel rod geometry. Grid and vane heights are the bottom of the features.

	(mm)
Total length	3894.4
Active fuel length	3657.6
Pellet radius	4.096
Gap width	0.084
Clad thickness	0.57
Spacer grid height	38.1
Mixing vane height	20.0
Grid 1	604.51
Grid 2	1166.22
Grid 3	1719.85
Vane 1	2015.89
Grid 4	2273.48
Vane 2	2569.53
Grid 5	2827.11
Vane 3	3123.16
Grid 6	3380.74

Figure 1. A representation of the 2D RZ mesh. **(a)** Plenum. **(b)** Spacer grid. **(c)** Base of the rod.

There were challenges with adding the assembly structural features to the fuel rod simulation, ultimately resulting in convergence issues. Therefore, the standard boundary conditions were modified to address these challenges. Firstly, the thermal contact model was reworked to include options for explicit and partially explicit formulations where both or one of the surfaces (inner clad or outer fuel pellet) use the values from the previous timestep. To compensate, smaller timesteps were used especially during the LOCA portion of the simulation where the timestep size (dt) was limited to 4 ms or less.

The second modification was to record the previous two timestep values of the gap distance between the fuel and cladding. Thus, when nodes sometimes lost contact with their nearest neighbor on the opposing surface, the last recorded value would be used instead. Typically, within a few timesteps, contact is reestablished, and the model resumes using the values from the current time step. This prevented hot and cold spots from forming on the fuel and clad, respectively.

The third modification is related to the second but is for the opposite (inner clad or outer fuel pellet) surface temperature. Postprocessors were used to record the average temperatures of the inner cladding surface in 100 mm increments. Then those values were imported into the thermal contact model. This allowed for consistent heat flow across the pellet/clad gap. While not essential for 2D, this modification was performed due to the difficulty in establishing contact between the cladding and spacer grids in 3D. A penalty Dirichlet boundary condition was generated to prevent the cladding from expanding beyond a specified radius within specified axial regions. Thus, the physical constraint of the spacer grids could be imposed without meshing and modeling the spacer grids explicitly. Figure 2 shows an example 24 mm tall segment of fuel and cladding with the boundary condition active on the middle 13 mm of the segment. The first image shows the cladding is allowed to creep down onto the fuel during operation. The second image shows the cladding is restrained from expanding past a radius of 4.755 mm, where the boundary condition becomes active.

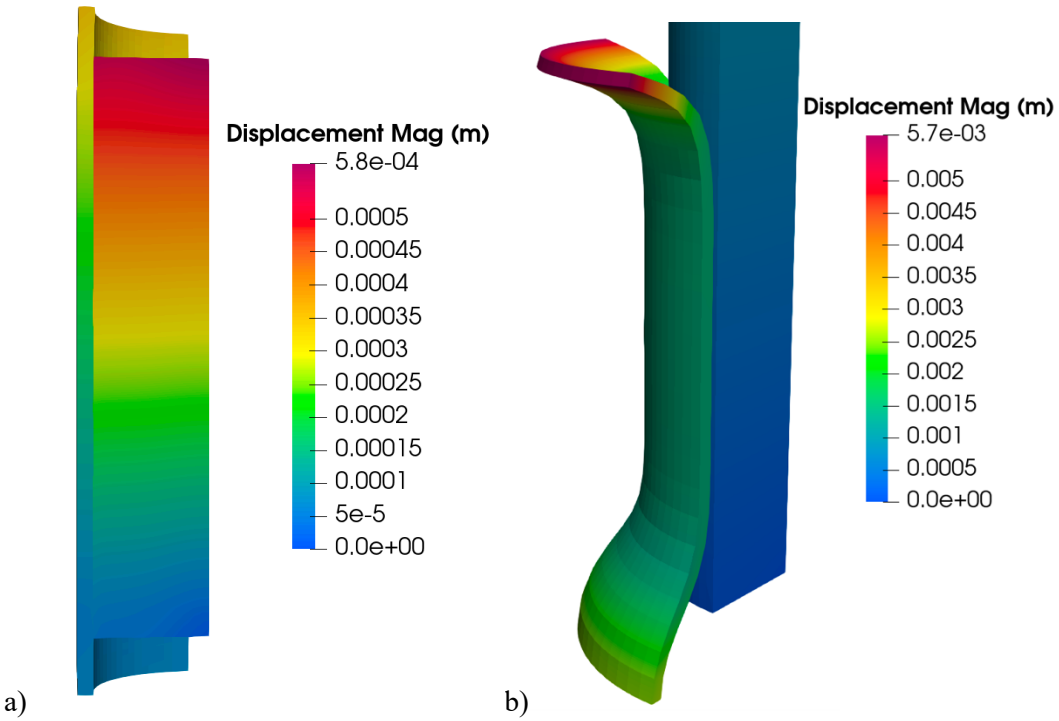

Figure 2. Example using a boundary condition to enforce the restraint of a spacer grid. **(a)** Shows that the boundary condition does not prevent the cladding creeping down onto the fuel, and **(b)** the cladding expands from the fuel, but part of the cladding is restrained by the boundary condition. This is extreme deformation for model testing purposes.

The 3D simulations in this work are a quarter rod. A full rod with realistic spacer grids and mixing vanes was planned but was unsuccessful due to convergence issues. The 3D quarter rod simulations reuse the 2D coolant temperature and power histories since circumferential symmetry is necessary for a 2D to 3D comparison. Also, the 2D and 3D simulations were adjusted to use the same boundary condition to allow for a more valid comparison.

This work specifically looks at high-burnup fuel rod performance; therefore, a fuel rod was selected from [2, 4, 5, 6] for the analysis. The fuel rod in question experienced two cycles of irradiation spanning 48 months of irradiation; see Figure 3. The power history also included a 27-day refueling outage. The LOCA event was set to occur at the last hot full power set point. VERA-calculated axial power profiles were applied to generate the time- and spatially dependent axial power distribution. VERA also provided the time- and spatially dependent cladding temperature during the steady-state irradiation; see example in Figure 4. TRACE was used to generate the detailed LOCA thermal hydraulic temperature profile.

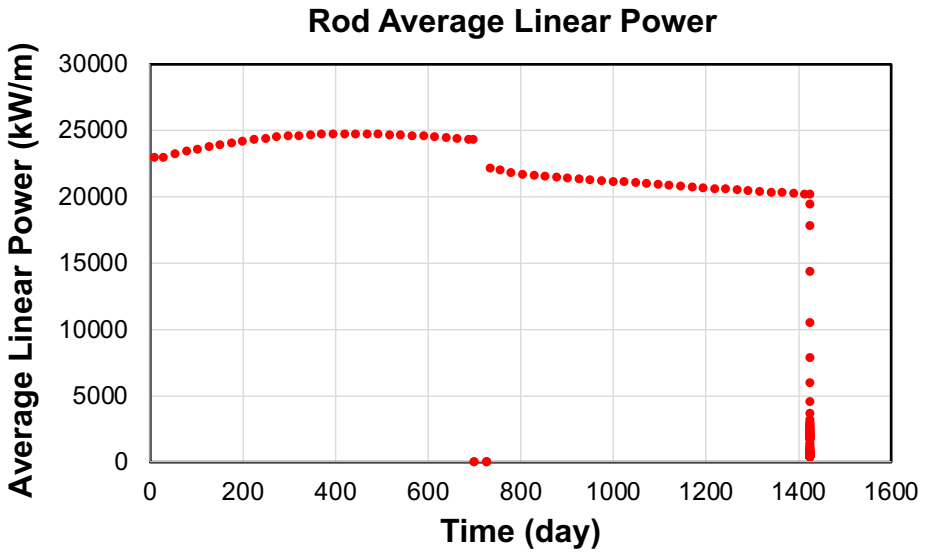

Figure 3. Plot of the rod average linear power vs. time.

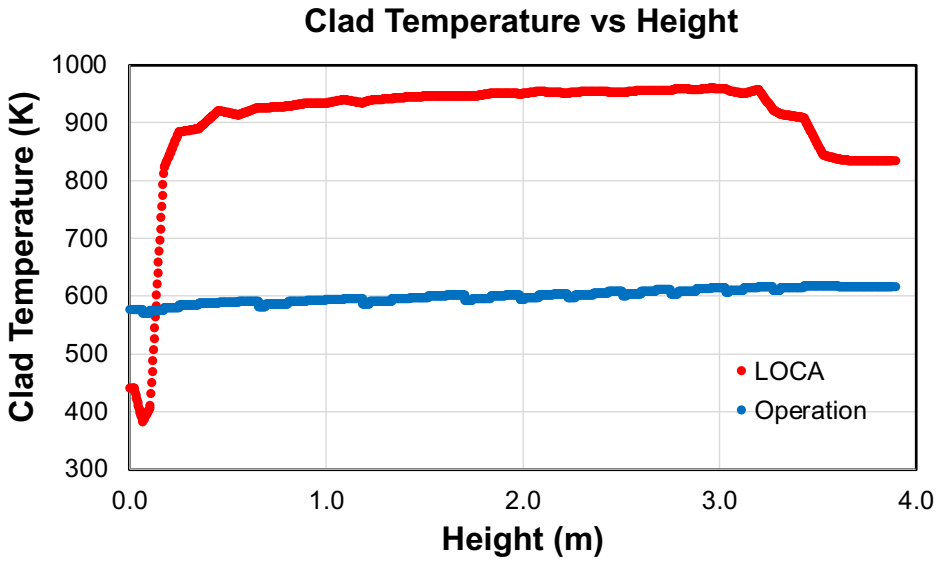

Figure 4. Plot of an example cladding temperature vs. height behavior during normal operation and the LOCA.

4. RESULTS

Cladding rupture is dependent on the fuel rod conditions at the time of the transient and thermal hydrulic conditions experienced by the fuel. Fuel rod failure typically occurres during the decay heat temperature rise that occurs after the blowdown phase of the LOCA, however, failure may ocurre during the initial heatup phase of the transient. Therefore, three cladding failure criteria were considered in this analysis to capture all failure mechanisms and ensure conservatism. The first is the rupture temperature, which depends on the heating rate (dT/dt) and the hoop stress [21]. The second is the overstrain criterion, which is a constant 0.336 hoop creep strain [19]. The third is a creep strain rate limit, which is fixed at 2.78×10^{-2} s^{-1} [19]. The simulations in this work were terminated after the cladding ballooned 4.75 mm (19 mm max diameter). However, the predicted time for burst using the rupture temperature, over strain, and strain rate criterion were recorded and compared when considered relevant.

This activity was carried out to build upon and compare results with those of previous work [25]. However, a new mesh had to be generated to capture the mixing veins and spacer grids, and the results had to be compared to the previos results to ensure consistency. The results of these comparisons can be seen in the figures below. Figure 5 compares the hoop stress and strain betweeen the original mesh and the new mesh, Figure 6a shows the results of the original simulation with internal mesh generation Figure 6b shows the sresults for the mesh generated in Cubit for the purposes of adding grid spacers and mixing veins to the meshed geometry. Therefore, the max radial displacement will be the same at the end of the simulations. However, the timing of the end of the simulation, balloon shape, and location of the balloon can be different. However, the difference is fairly small and considered negligible. The only observable difference is the stress on the cladding. There did, however, appear to be a difference in the axial balloon geometry. The results of the original simulation and the Cubit mesh comparison show that the axial balloon is somewhat longer in the Cubit mesh, and the stresses are somewhat different. This is believed to be related to the mesh fidelity; therefore, a mesh sensitivity study was performed.

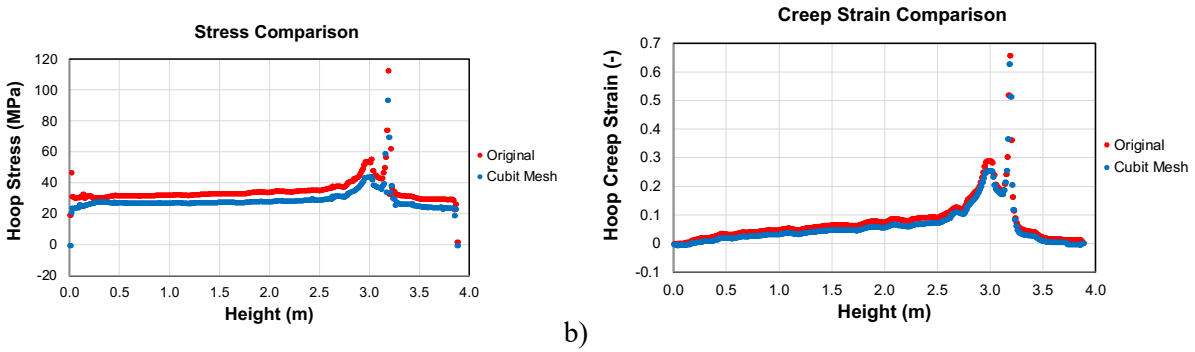

a) b)

Figure 5. Plots of the hoop stress and hoop creep strain comparing the **(a)** original and **(b)** cubit generated mesh at end of simulation.

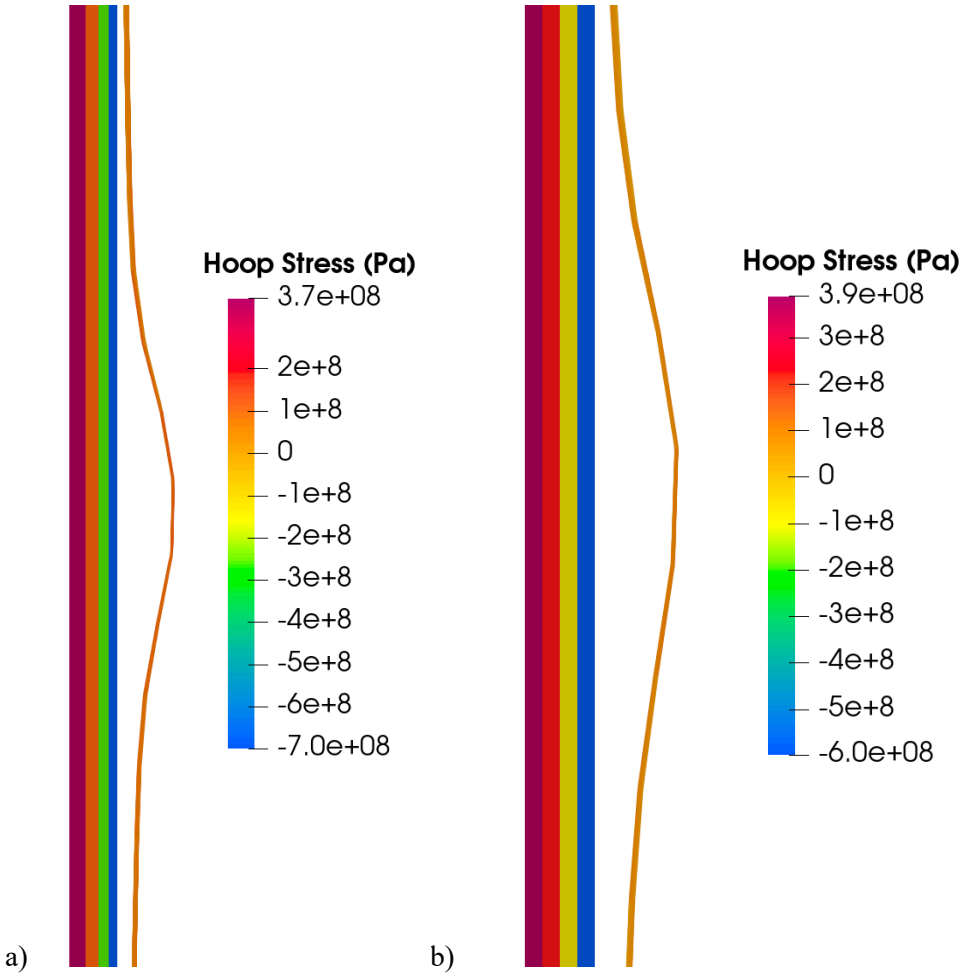

Figure 6. (a) Original simulation with internal mesh generation. **(b)** Original simulation recreated with a mesh produced in Cubit. Hoop stress profile in the fuel and cladding. Maximum radial displacement is 4.75 mm in both cases.

The results of the mesh sensitivity study are shown in Figure 7 summarizes the results of the mesh sensitivity study. The study consisted of varying the number of axial mesh elements between 300 and 1,500. Each mesh in the study assumed three radial elements and is not expected to impact the balloon strain or stress behavior. The results indicate that an axial mesh of 600 to 900 are sufficient to capture the cladding behavior. The hoop stress profile improved when the number of axial elements increased, as can be seen in Figure 7 a), b), and c). However, this behavior eventually saturated out as the fidelity as the axial mesh increased to 900 elements, see Figure 7 c), d), and e). The hoop creep strains are plotted in Figure 8. Figure 8 shows the convergence of the creep strain with increasing mesh density over the length of the rod and verifies the results in Figure 7.

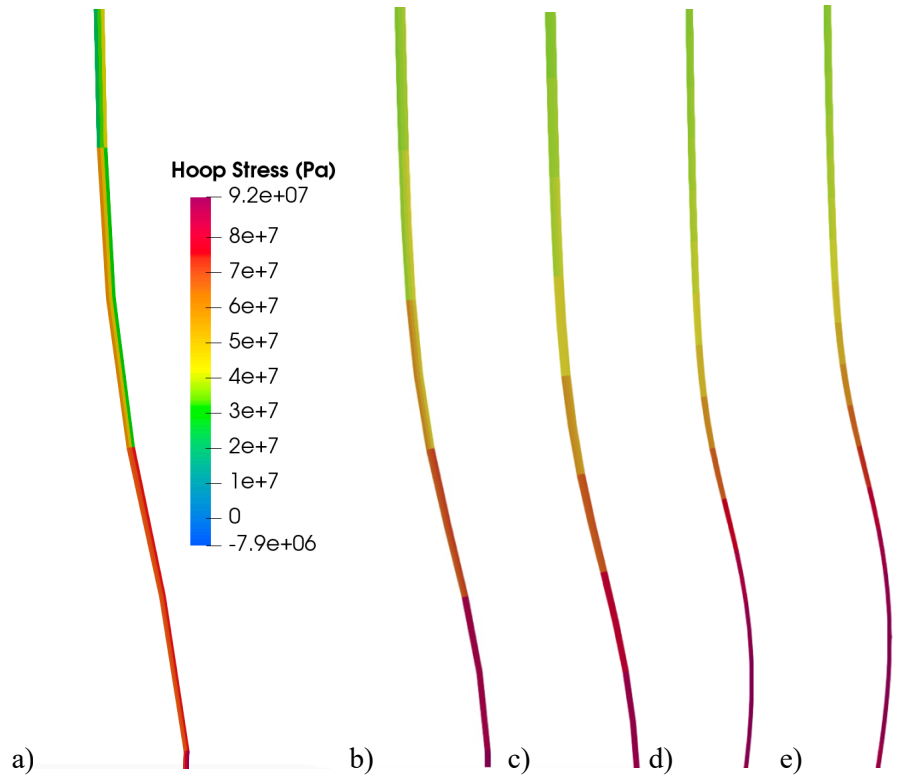

Figure 7. Mesh sensitivity study. **(a)** 300 axial elements, **(b)** 600 elements, **(c)** 900 elements, **(d)** 1200 elements, **(e)** 1500 elements. The maximum stresses are 92, 85, 84, 84, and 84 MPa for the 300 to 1500 element case respectively.

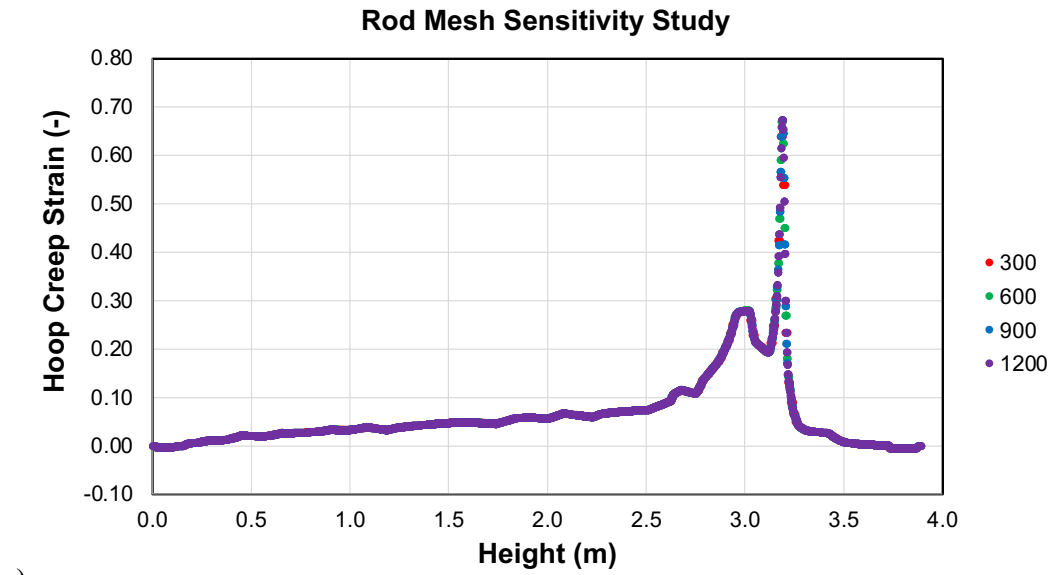

a)

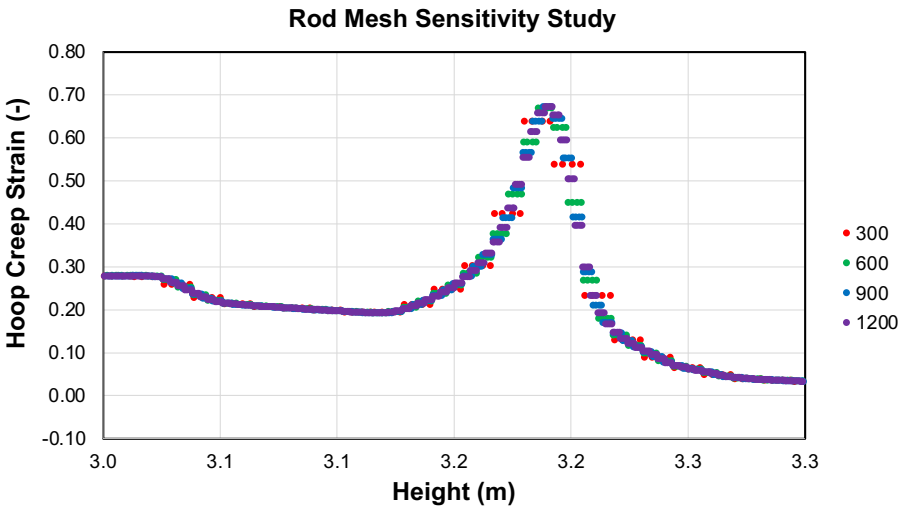

b)

Figure 8. Plot of the hoop creep strain at the end of the mesh sensitivity study. **(a)** Overview. **(b)** Close up of the balloon region.

Axial spacer grids and mixing veins were then applied to the new mesh after it was verified that the new mesh was comparable to the original mesh. The results of the cladding performance with the assembly structural features are shown in Figure 9. The grids are effective at locally suppressing the clad ballooning in their localized areas. However, the grids are ineffective at preventing the cladding from bursting or significantly delaying the burst time.

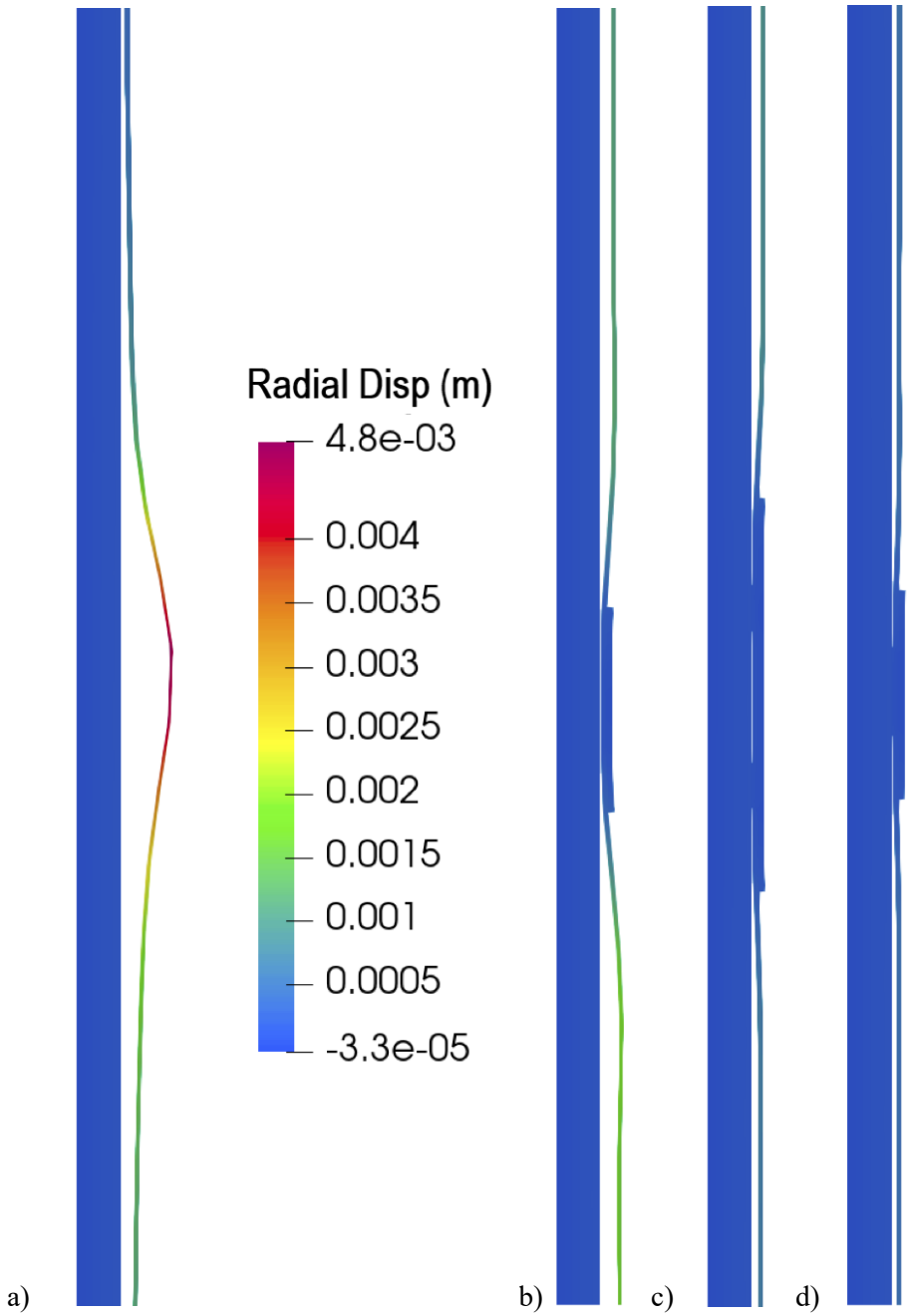

Figure 9. Cladding displacement with grids. **(a)** Burst location. **(b-d)** Top three spacer grids.

The assembly structural features are typically made up of a zirconium alloy (Zircaloy) or Inconel material. Inconel is a stronger material than Zircaloy. However, at these elevated temperatures, both materials would be subject to deformation as a load is applied, and, therefore, it is important to capture this behavior to correctly calculate the cladding performance, and overall system performance. Mechanical clad–grid contact was applied to the outer clad and inner grid surfaces. The axial position of grids was maintained with the Dirichlet boundary condition. Convective heat removal via the coolant was set on the inner and outer grid surfaces. Thermal contact for the grids was neglected because the clad is in contact with the grids only during the LOCA, and therefore, the grid temperatures are set to the coolant temperatures predicted by the thermal hydraulic codes. Coolant pressure was also neglected because it

applies to both sides of the grid. This behavior can be observed in Figure 10. The spacer grids begin bowing radially outward as the cladding begins to balloon. This result highlights the effect of the spacer grid on the balloon and confirms that the spacer grids were not rigid. Again, the clad hoop creep strain for this study is shown in Figure 11. This shows the convergence of the mesh as it is increasingly refined.

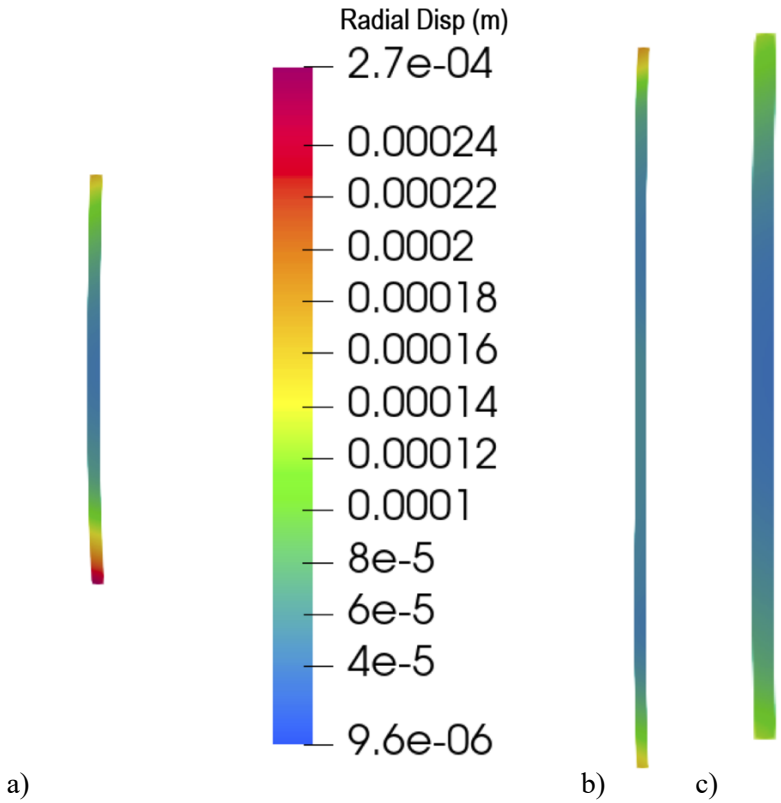

Figure 10. Grid displacement. **(a-c)** Top three spacer grids in order from highest to lowest.

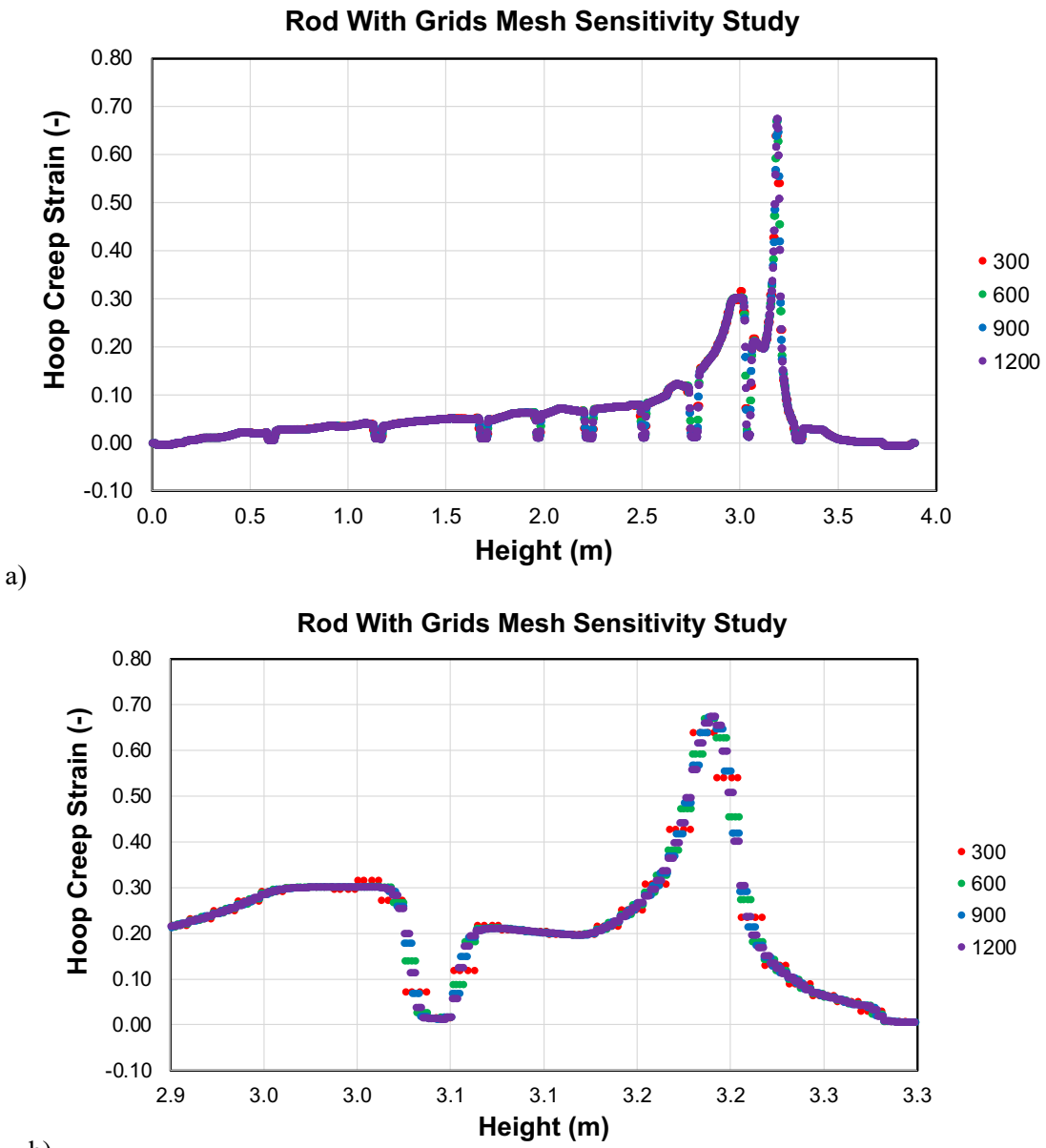

Figure 11. Plot of the clad hoop creep strain from the sensitivity study with grids. **(a)** Overview. **(b)** Close up of the balloon region.

Another important consideration is the interaction between the cladding and grid spacer / mixing vein. Therefore, a cladding mesh sensitivity study was performed to evaluate the local stress behavior of the cladding as it interacted with the assembly structural features. The results of the sensitivity study can be seen in Figure 12. The stress in the assembly features is of little concern, as the purpose of this study is to investigate the cladding performance. Therefore, the spacer grids were given constant 24 axial elements. This axial distribution results in the axial mesh distribution in the assembly feature being smaller than the cladding. The cladding axial mesh distribution was varied between 300 and 1500 axial elements, and, similar to the previous results, the mesh refinement converges at 900 axial cladding elements.

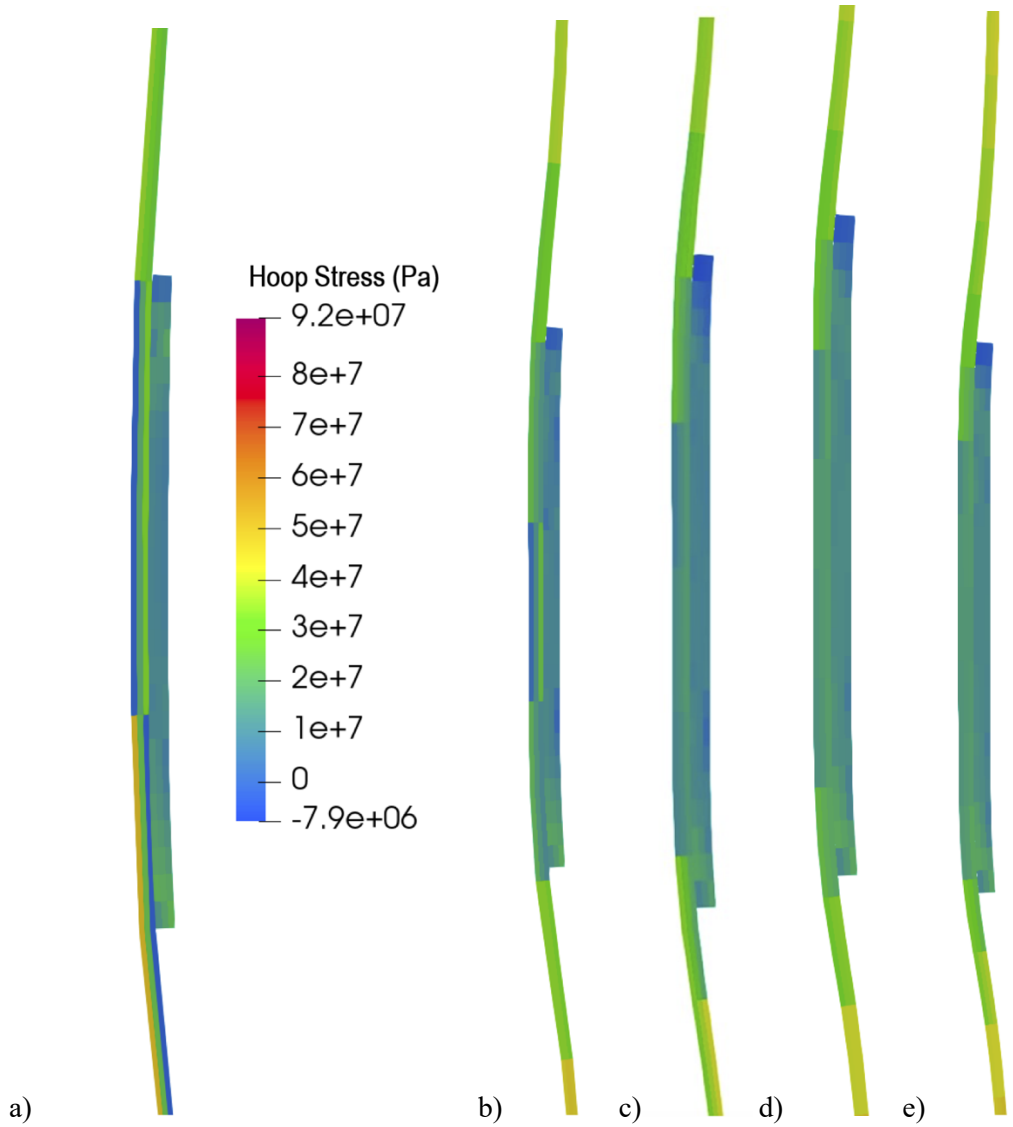

Figure 12. Mesh sensitivity for the grids. **(a)** 300 axial elements, **(b)** 600 elements, **(c)** 900 elements, **(d)** 1200 elements, **(e)** 1500 elements. The maximum stresses are 92, 85, 84, 84, and 84 MPa for the 300 to 1500 element case respectively.

A set of simulations was also considered to evaluate opportunities to reduce ballooning or shift the burst location to a more favorable location (lower burnup). Three additional simulations were considered. The simulation labeled as "rod" refers to the simulation without spacer grids, "grid" considers the nominal cladding and spacer grid configuration, "adjusted" assesses the impact of spacer grid location by moving one to the burst location from the previous "grid" case, "long grid" increases the top spacer grid length from 38 mm to 650 mm, and "thick clad" doubles the cladding thickness to 1.2 mm along the entire rod while maintaining nominal spacer grid locations and lengths. Table 3 shows the burst times and heights for the various spacer grid configurations. The time to burst decreases by 5 s, and the burst temperature decreases by 30 K when the assembly structural features are added. This decrease in burst time appears associated with the constraint imposed by the structural features. The spacer grids reduce the displacement in localized areas, which reduces the total possible volume expansion of the cladding thereby producing somewhat higher gas pressures. Additionally, the displacement is concentrated in areas away from the spacer grids which produces a more rapid rupture. The thicker cladding has a longer burst

time due to the lower stress afforded by the increased thickness. The burst temperature is the cladding at burst which is controlled by the coolant temperature history.

Table 3. Burst results for various spacer grid configurations using rupture temperature criterion. Zero height is at the bottom of the cladding tube.

	Time to Burst (s)	Burst Height (m)	Burst Temp (K)
Rod	50.8	3.200	1081
Grid	45.6	3.016	1057
Adjusted	45.6	3.025	1057
Long grid	41.3	2.905	1035
Thick clad	74.0	3.178	1114

The cladding creep strain at the respective burst times is plotted in Figure 13. The axial clad temperature reliably increases with height (see Figure 4) to the point where the linear heat rate peaks and then decreases. Thus, the creep strain is greatest in the upper areas of the cladding. The effect of the assembly structural features can be seen in the creep strain plot as the sudden and localized strain decreases. The minor decreases in the creep strain for the "rod" (without grids) is due to the local depression in heating in those areas, as the power and coolant temperature data are based on VERA depletion results considering the structural features' impact on burnup suppression. The sudden drop in creep strain for the "long grid" case at about 2.9 m is due to the 650 mm tall top spacer grid effectively reinforcing the top part of the cladding. However, this partial reinforcement did not improve the burst time.

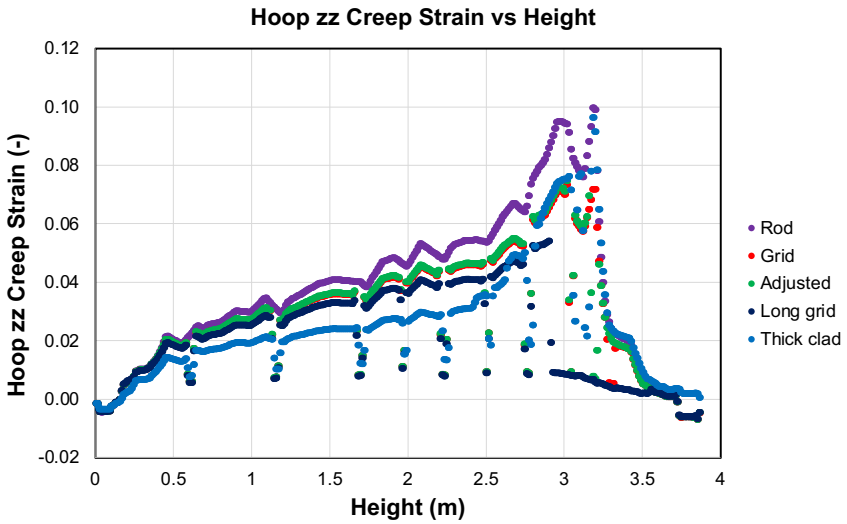

Figure 13. Cladding creep strain as a function of axial position

The displacements for each simulation are shown in Figure 14. The most interesting result was recorded when a spacer grid is moved over the nominal burst location. In this simulation, the balloon is unable to form in the preferred location; therefore, competing balloons form, resulting in BISON predicting a double balloon. In the case of the 650 mm tall grid, the balloon is predicted just under the top grid. In the

thick cladding case, the balloon is predicted below the top grid. The cause of the balloon location shifting from 3.016 to 3.178 m is unclear, but it may be due to the thicker cladding applying a larger axial restraint due to the larger 2× radial to axial ratio.

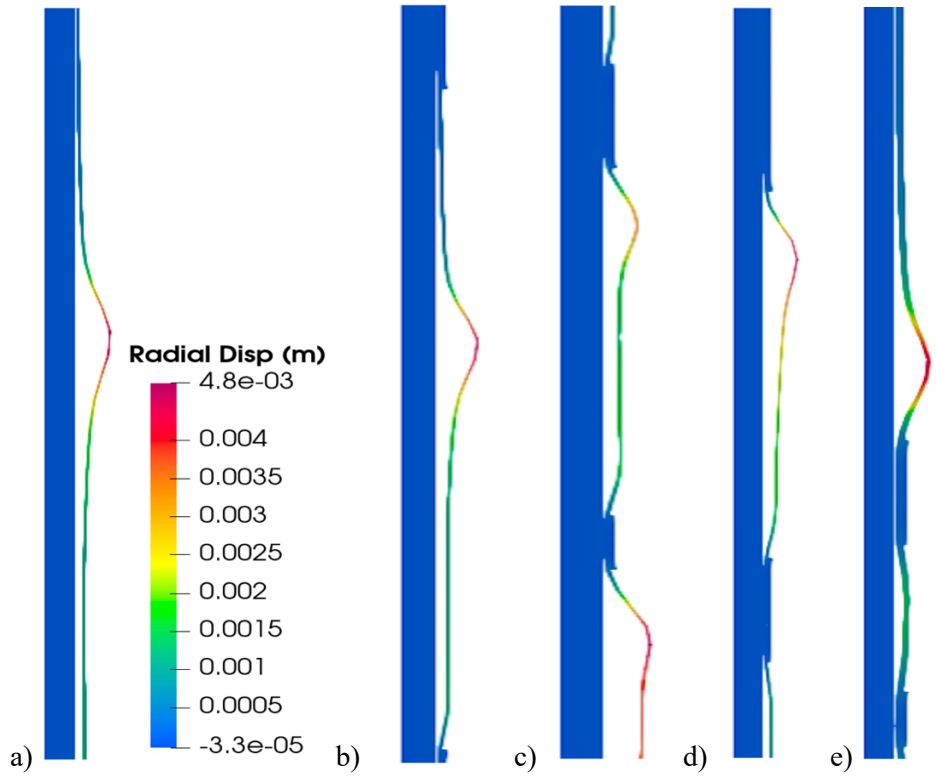

Figure 14. Cladding displacement for various spacer grid configurations. Radial direction is exaggerated for visibility. **(a)** No grid contact, 3.2 m. **(b)** Nominal grid condition, 3.016 m. **(c)** Spacer grid moved to nominal burst location, 3.025 m. **(d)** Top spacer grid 650 mm tall, 2.905 m. **(e)** Cladding 2× thicker compared to nominal case, 3.178 m.

The impact of cladding burst criteria was also considered, as it may affect the simulation results. Two cladding failure criteria were considered: (1) the Chapman model [26] and (2) overstrain criteria [19]. A comparison of the simulation results can be seen in Figure 15, which summarizes the hoop creep strain at end of the simulation. The end of the simulation is when the cladding balloons to a 4.75 mm radial displacement.

Table 4 lists the burst time predicted for each failure mechanism.

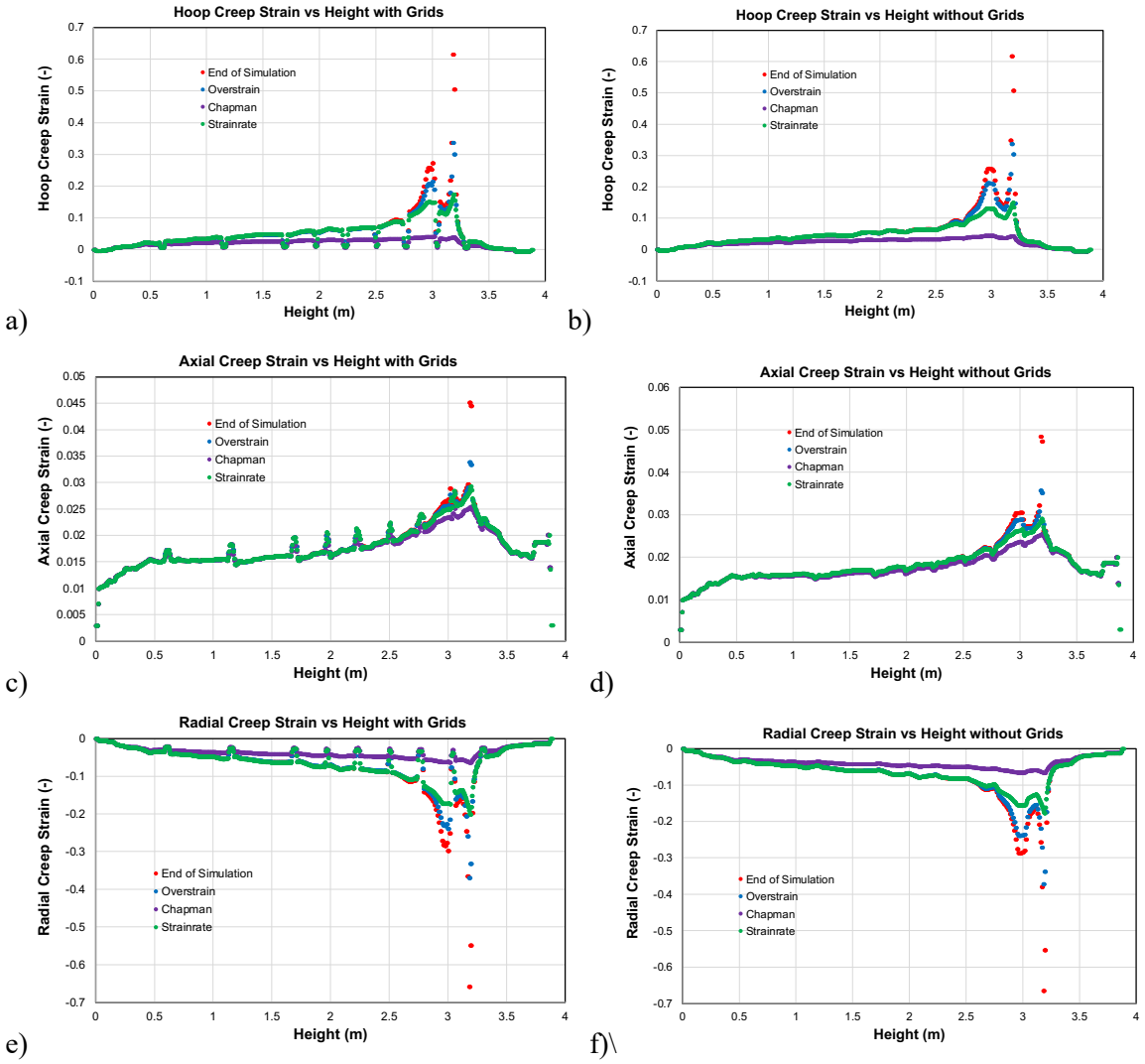

Figure 15. Plot of creep strain at end of simulation, burst time using Chapman correlation for rupture temperature, and overstrain which it the 33.6% ultimate tensile strain. **(a, c, and e)** With spacer grids. **(b, d, and f)** Without spacer grids.

Modifying the cladding burst criteria affects burst timing and temperature, but it also affects the cladding temperature profile. The clad temperature at the failure times is plotted in Figure 16. The rupture temperature criteria are clearly the most conservative failure model, resulting in failure occurring in the early stages of reflood. It should be noted that the effects of oxidation or oxygen content in the fuel were

not included in this work. However, delaying failure results in additional reflooding to occur, and although this will not significantly affect limiting relocation, experimental data suggest that hydrostatic pressures can reduce fuel fragmentation. Therefore, increasing the cladding rupture temperature may ultimately reduce fuel susceptibility to dispersal as less fuel will fragment into small fragments.

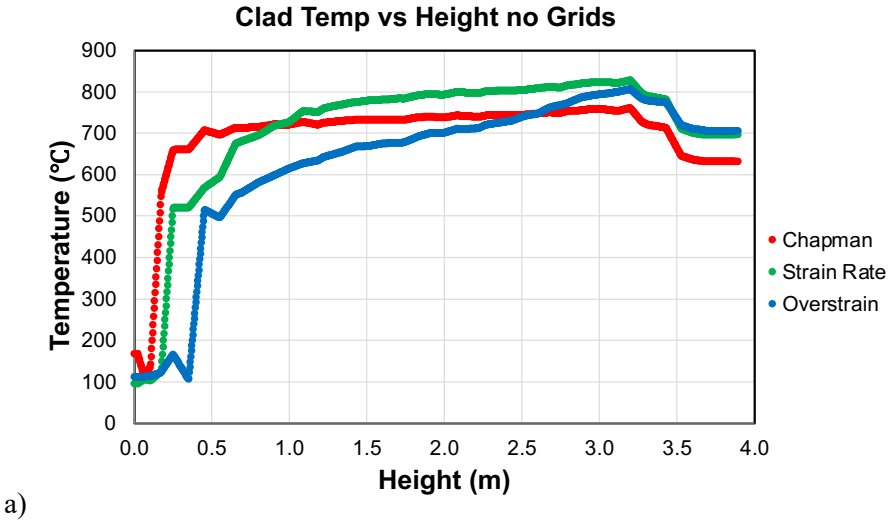

a)

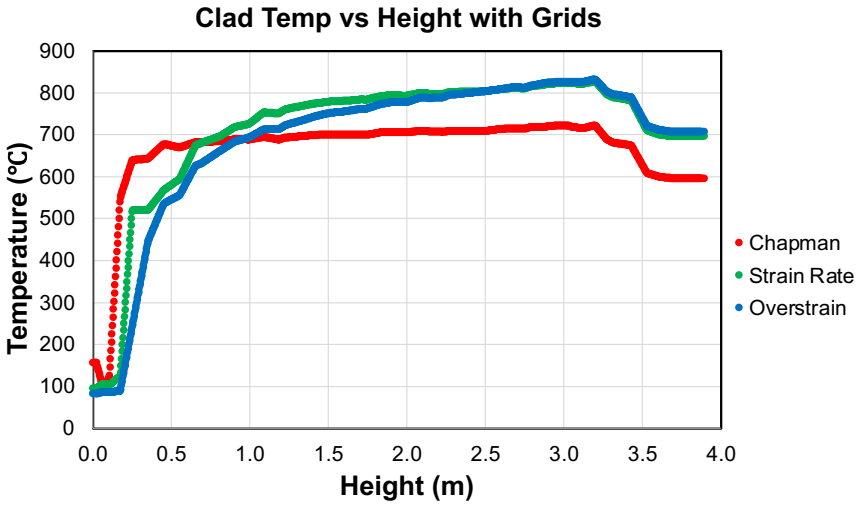

b)

Figure 16. Plots of the cladding temperature at the failure times for **(a)** without the grids, **(b)** with the spacer grids.

The creep strain rate failure criterion narrowly avoids being reached early in the LOCA due to the very rapidly changing conditions and relatively small rate limit. However, the creep rate reaches a maximum during the balloon stage of the accident. The rupture temperature criterion is based on the heating rate (temperature time derivative) and the clad hoop stress. This limit is reached much later compared to the creep rate limit. The overstrain limit (33.6% strain) is reached at almost a minute and provides an upper bound for the burst time since this limit corresponds to the estimated ultimate tensile strain, which is the strain at the onset of plastic instability. Overstress or brittle failure is not expected for these conditions.

Table 4. Burst times for each criterion. Overstress failure was not predicted.

Failure Criterion	Grid Burst Time (s)	Rod Burst Time (s)
Creep Strain Rate	55.02	55.02
Rupture Temperature	33.14	40.22
Overstrain (ultimate tensile strain)	58.72	61.37
Overstress (brittle fracture)	—	—

Figure 17 shows the radial displacement, clad temperature, hoop stress, and creep strain profiles around the balloon location near the top of the clad. The spacer grids can reduce the creep strain and hoop stress in their local areas. The key takeaway is that they do not negatively impact the overall balloon and burst behavior of the cladding. Additionally, FFRD will be limited to the region between the assembly structural features.

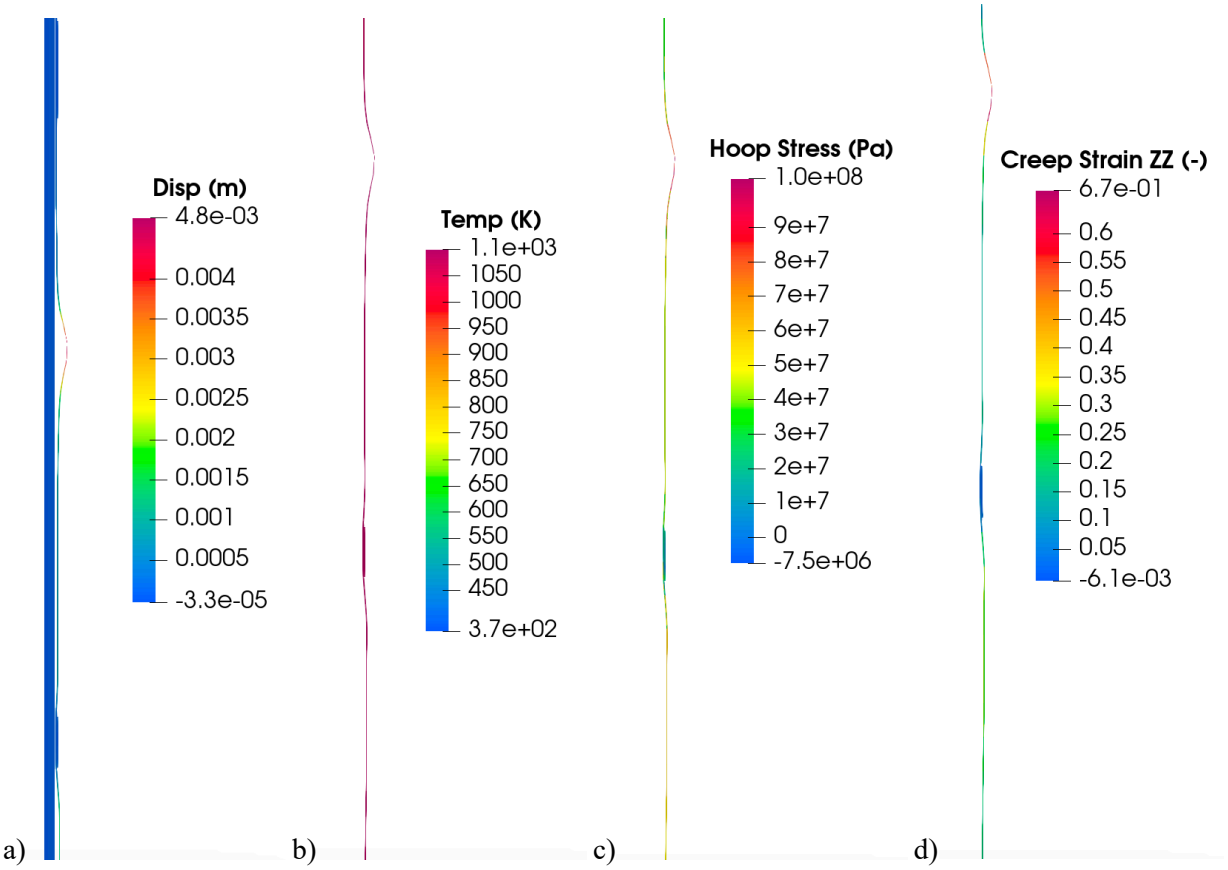

Figure 17. Profiles at end of simulation. **(a)** Radial displacement. **(b)** Temperature. **(c)** Hoop stress. **(d)** Hoop creep strain.

The effect of initial rod internal pressure (RIP) was considered, and the results of these simulations are summarized in Figure 18 and Figure 19. Figure 18 characterizes the results for the simulations with the assembly structural features, whereas the results shown in Figure 19 do not consider the assembly structural features. Both studies leveraged the strain rate cladding failure criteria, as it has been shown to predict cladding rupture temperatures more accurately. The general trends are as expected and show the results were very similar to those previously presented. Failure occurred at 3.1 to 3.2 m from the bottom of the rods and a secondary concentration at about 3 m. The key takeaway from Figure 18 is that the cladding performance with the assembly features were not affected by the initial RIP.

The hoop and radial creep strain directions are expected for an internal gas pressure. However, the additional axial creep strain at the spacer grid locations appears to be the result of the cladding bending at the ends of the spacer grids. The strain rate limit is reached earlier, above about 6 MPa initial fill pressure. Thus, the hoop and radial strains decrease. However, it was interesting to note that the axial strain reaches a maximum for a 6 MPa RIP. The creep strain at strain rate failure for the rods without spacer grids is shown in Figure 19. The results are fairly similar to those with the spacer grids. However, there is the notable lack of major discontinuities from the spacer grids.

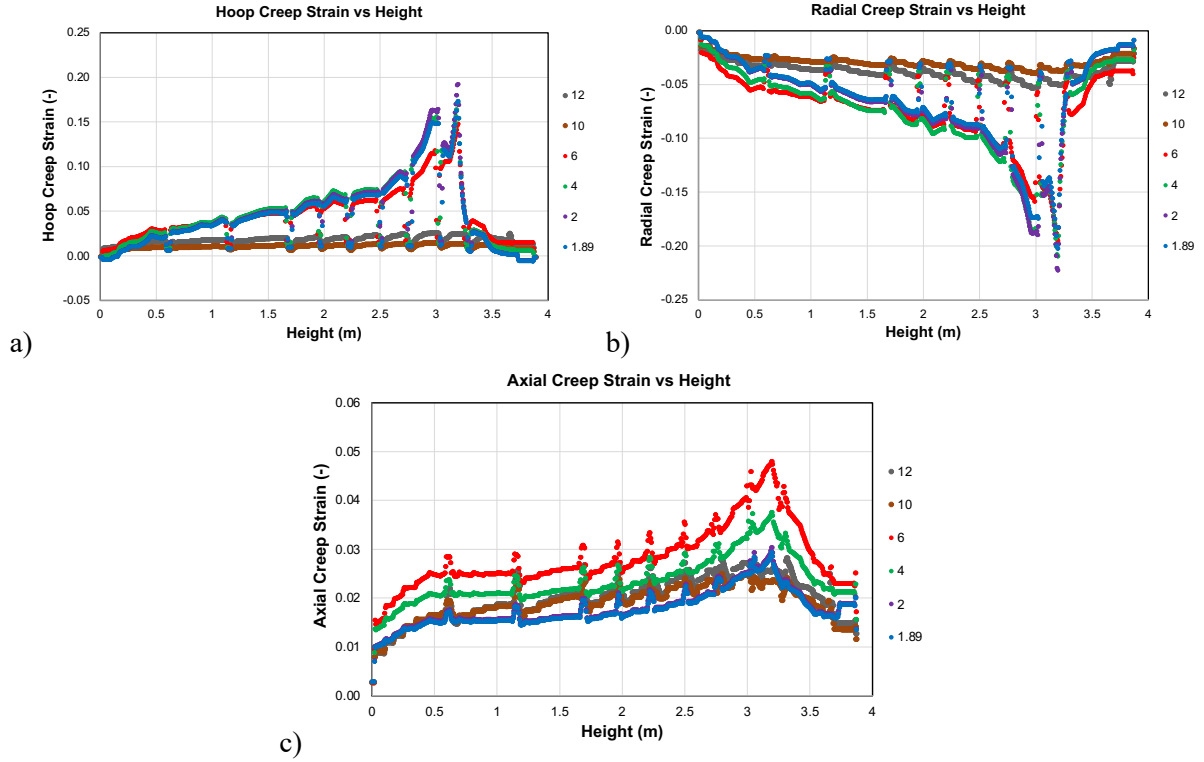

Figure 18. Plots of the **(a)** hoop creep strain, **(b)** radial creep strain, and **(c)** axial creep strain at strain rate failure with increasing rod initial fill pressure.

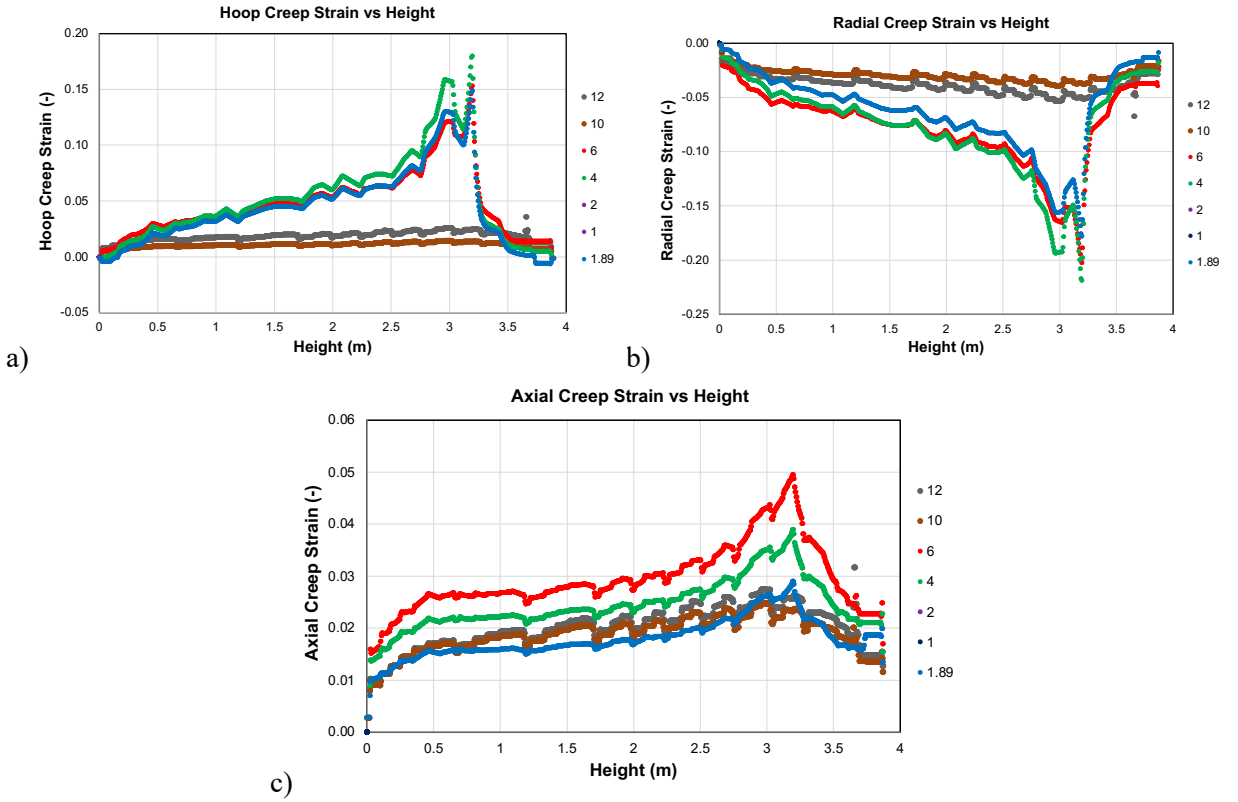

Figure 19. Plots of the **(a)** hoop creep strain, **(b)** radial creep strain, and **(c)** axial creep strain at strain rate failure with increasing rod initial fill pressure.

4.1 3D SIMULATIONS

Due to convergence and computational time issues, the quarter rod simulation was started about 115 days before the LOCA event. This does affect the final results, especially in the time to burst. The primary difference is that the gas pressure at the LOCA onset is only 4.4 MPa for the quarter rod but 14.0 MPa for the 2D rod due to the difference in fission gas release and burnup. There were other differences such as the fuel being in contact with the cladding for the 2D case, but not for the 3D case. This led to an 80–100 K higher average fuel temperature for the 3D case. However, the clad temperature was nearly identical.

However, the simulation did predict a balloon, and spacer grid boundary conditions did constrain the cladding in their respective regions. Some results from a quarter rod simulation are shown in Figure 20 and Figure 21. The burst location was at about 3.16 m, which is somewhat higher than those predicted by 2D simulations and the creep strain at lower heights is smaller than those previously predicted. Presumably, this may be due to different start time. However, the overall shape of the profiles is consistent with those predicted by the 2D simulations. Table 5 compares the burst times of the 3D and 2D simulations. It is presumed that the 2D simulations are more representative due to the 2D simulations including the operation phase of the simulation.

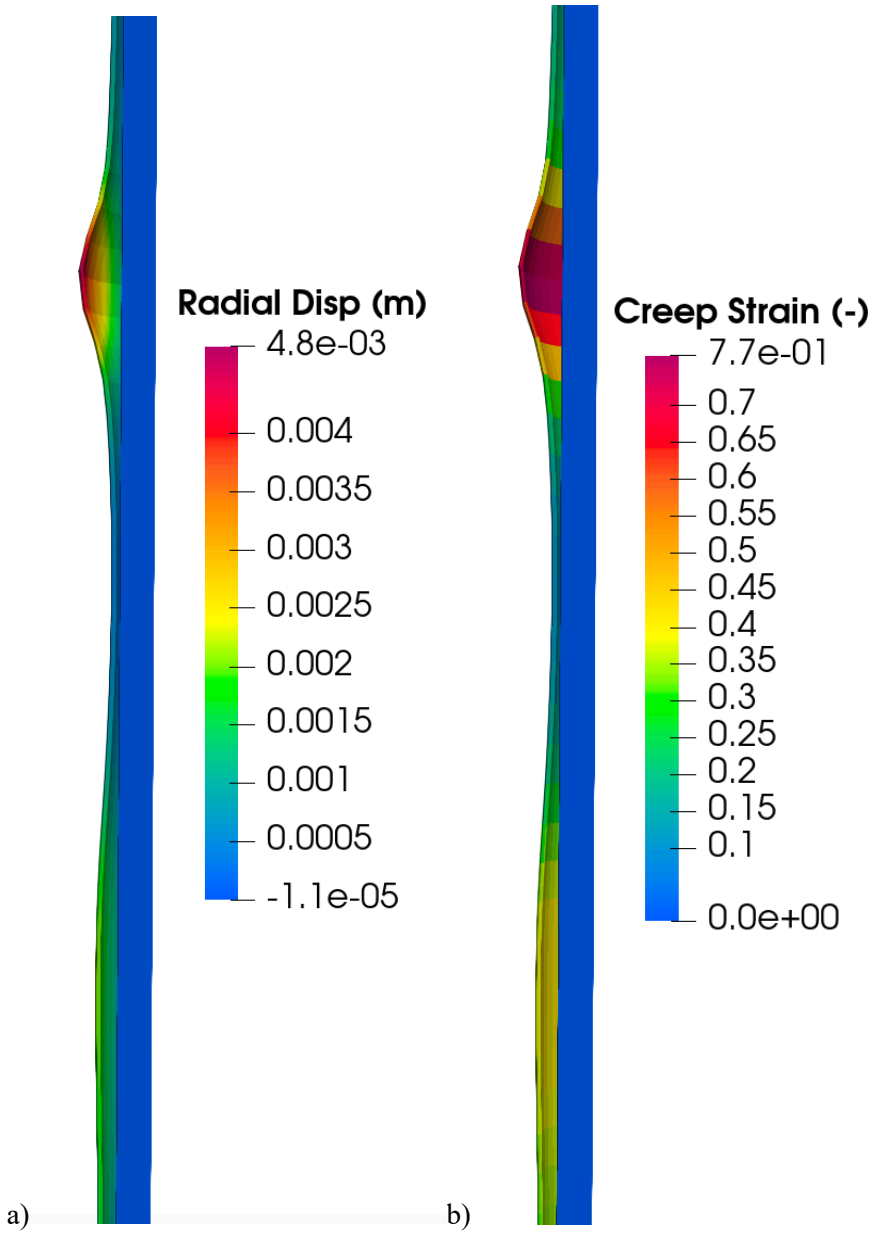

Figure 20. Quarter rod with grid boundary condition results. **(a)** Radial displacement and **(b)** creep strain magnitude.

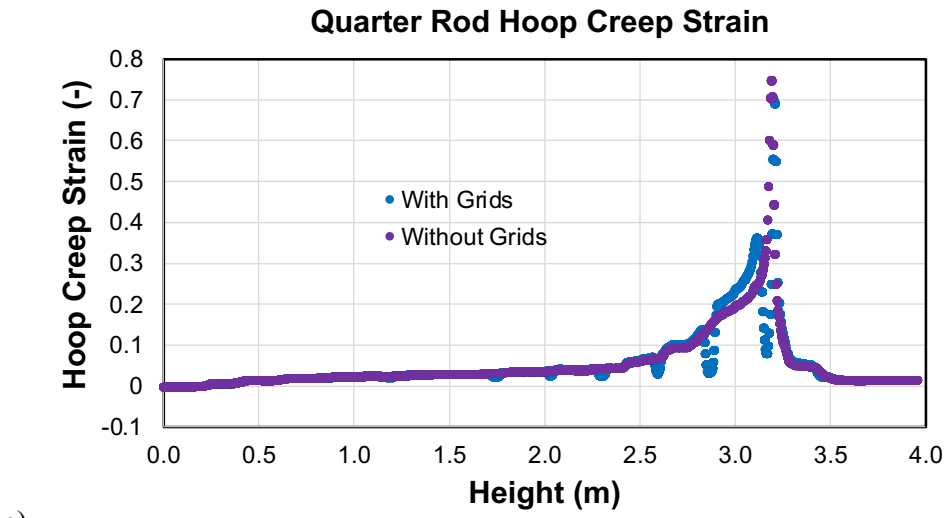

a)

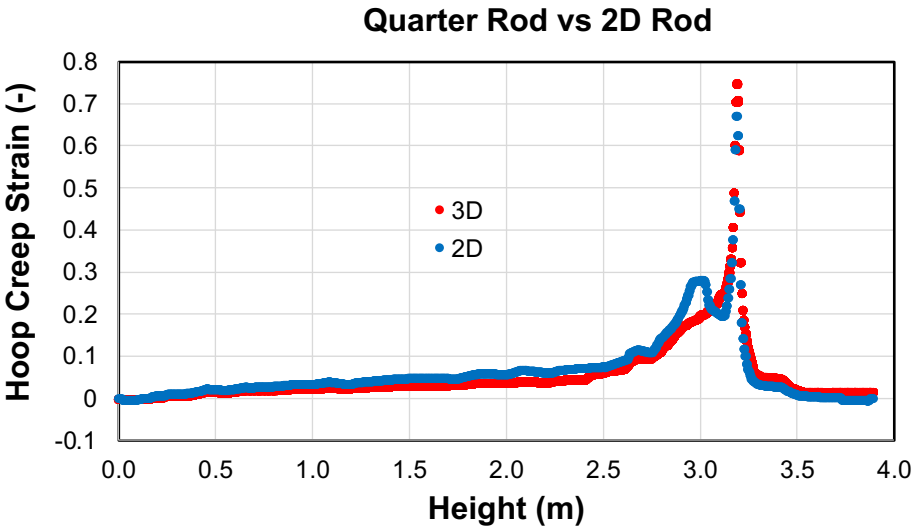

b)

Figure 21. (a) Plot of the hoop creep strain for the quarter rod at end of simulation with and without spacer grids. **(b)** Plot comparing 2D and 3D results without grids.

Table 5. List of burst times.

	3D without grids (s)	**3D with grids (s)**	**2D without grids (s)**	**2D with grids (s)**
Strain Rate	76.85	76.33	55.02	55.02
Rupture Temperature	58.01	58.36	40.22	33.14
Overstrain	78.33	77.51	61.37	58.72
Overstress	-	-	-	-

5. DISCUSSION

A major assumption in the previous assessment [5, 6, 7] is associated with the effects of the assembly structural features on FFRD. FFRD was assumed to be limited to the axial region between assembly structural features. However, the assembly structural features were not explicitly modeled, resulting in the local cladding strain exceeding the cladding strain threshold outline in the NRC RIL [2]. This work intends to address this technical gap and investigate the assumptions' validity.

The original simulation results were duplicatable with a Cubit mesh for the purposes of including the assembly structural features in the mesh, and the mesh was refined based on the results of the mesh sensitivity study. The grids did not require an additional boundary condition to maintain their radial position, and it was found that the grids locally depressed the clad deformation and temperature. The time to burst and burst temperature decreased somewhat due to the spacer grids concentrating the displacement in certain areas of the clad. A point of note is spacer grids were allowed to mechanically deform and were not fixed in place thereby unrealistically restricting cladding displacement. Therefore, spacer grids, at least of traditional designs, appear not to negatively impact balloon burst behavior or impact; however, the spacer grids do locally limit ballooning and limit FFRD to the region of fuel between the spacer grids.

The effect of the grids can be clearly seen in the sudden and local reductions in hoop and radial creep strains. The axial creep strain increased in the region in which the spacer grids were located. This appears to be due to the neighboring areas experiencing comparatively greater deformation and axially pulling the cladding located under the grid. It was also noted that the location of the grids did affect the burst location. However, increasing the time to burst was not achievable without major modifications to the spacer grids. Thus, it may be possible to use the spacer grids to direct the burst to a more desirable location to mitigate the effects, but the event cannot be prevented with this technique.

The effect of rod initial pressure was considered, and it was found that the RIP reduced the creep strain at burst when using the rupture temperature criterion. The overstrain criterion, since the failure strain limit is constant, did not see any changes at burst. However, it was noted that the predicted axial and radial strains increased with higher RIPs.

Simulations in 3D proved to be difficult and computationally expensive. Although full 3D rods with grids were planned and seemed doable, convergence was found to be a continual problem. It remains somewhat unclear as to the cause of the convergence issues. However, it appears to be related to the gap contact combined with the relatively high creep rate of the cladding. There is also an issue with the thousands of timesteps required for these simulations and size of the 3D meshes. A first-order full rod with spacer grids is about 40 MB. It is expected that the simulation, if successful, would take about a month to complete. The mesh could be coarsened. However, based on the results of the mesh sensitivity study, this would reduce the accuracy of the results, which is the primary purpose of performing a 3D simulation instead of a 2D RZ simulation. Given the events with a single 3D rod, the 3×3 array of rods was not attempted. Overall, it was found that 2D RZ simulations are more practical for most purposes at this time.

6. SUMMARY

The Cubit based mesh was found to compare well to the original internally generated mesh. Spacer grids were added to the 2D RZ model and were found to both restrain the cladding and deform with the cladding. This provided confidence that the spacer grids were functioning as intended without the development of additional boundary conditions.

The effect of the spacer grids was about as would be expected. The spacer grid essentially acted to double the cladding thickness in local regions. The regions without a spacer grid were effectively thinner and more deformed compared to the spacer grid regions. Thus, the placement of the spacer grids could be used to limit FFRD to specific axial regions of the cladding. However, burst time was not significantly affected. Also, in 2D, the spacer grid is revolved around the cladding and thus has full contact with the entire perimeter of the cladding, which is different from an actual spacer grid that has contact at four points. As a result, the ability of the spacer grid to move the burst location would be more limited than the 2D simulations suggest. Also, the spacer grids did locally reduce the deformation of the cladding, which reduced the temperature locally in the fuel. However, the average rod temperature was not significantly affected.

3D simulations remain a topic for future work. The stability of the contact between the fuel–cladding and cladding–spacer grids is a convergence issue. Also, it may prove beneficial for the cladding models and UO_2 creep model to be more stable. Lastly, additional computational resources will be required for 3D simulations to be of realistic use for reactor design. As was found in the TCR program, models must be able to produce results within about three days for them to be effective for engineering purposes.

ACKNOWLEDGEMENTS

The simulations used the resources of the High-Performance Computing Center at INL, which is supported by DOE NE and the Nuclear Science User Facilities Program under contract no. DE-AC07-05ID14517.

7. REFERENCES

[1] U.S. Nuclear Regulatory Commission, "10 Code of Federal Regulations 50.46," [Online]. Available: https://www.ecfr.gov/current/title-10/chapter-I/part-50/subject-group-ECFRdf2af20f8a72d91/section-50.46. [Accessed 31 May 2023].

[2] U.S. Nuclear Regulatory Commission, "Regulatory Guide 1.174. Rev2," NRC, Rockville , 2011.

[3] F. Smith and R. Daum, "Alternative Licensing Approaches for Higher Burnup Fuel," EPRI, Palo Alto, 2020.

[4] R. Tregoning, L. Abramson, and P. Scott, "Estimating Loss-of-Coolant Accident (LOCA) Frequencies Through the Elicitation Process. NUREG-1829 Vol. 1," Nuclear Regulatory Commission, 2008.

[5] I. Greenquist, A. Wysocki, J. Hirschhorn, and N. Capps, "Multiphysics analysis of fuel fragmentation, relocation, and dispersal susceptibility–Part 1: Overview and code coupling strategies," *Annals of Nuclear Energy,* vol. 191, no. 109913, 2023.

[6] N. Capps, J. Hirschhorn, I. Greenquist, and A. Wysocki, "Multiphysics Analysis of Fuel Fragmentation, Relocation, and Dispersal Susceptibility–Part 2: High-Burnup Steady-State

Operating and Fuel Performance Conditions," no. http://dx.doi.org/10.2139/ssrn.4374144 , 2023.

[7] A. Wysocki, J. Hirschhorn, N. Capps, and I. Greenquist, "Multiphysics Analysis of Fuel Fragmentation, Relocation, and Dispersal Susceptibility–Part 3: Thermal Hydraulic Evaluation of Large Break Loca Under High-Burnup Conditions," no. http://dx.doi.org/10.2139/ssrn.4381361 , 2023.

[8] M. Bales, A. Chung, J. Corson, L. Kyriazidis, "Interpretation of Research on Fuel Fragmentation, Relocation, and Dispersal at High Burnup," U.S. NRC, Palo Alto, 2021.

[9] Idaho National Laboratory, "A Finite Element-Based Nuclear Fuel Performance Code," INL, 2023. [Online]. Available: https://mooseframework.inl.gov/bison/index.html. [Accessed May 2023].

[10] A. Marion (NEI) letter dated June 13, 2006 to H. N. Berkow (USNRC/NRR), "Safety Evaluation by the Office of Nuclear Reactor Regulation of Electric Power Research Institute (EPRI) Topical Report TR-1002865, "Topical Report on Reactivity Initiated Accidents: Bases for RIA Fuel rod Failures and Core Coolability Criteria"," http://pbadupws.nrc.gov/docs/ML0616/ML061650107.pdf, 2006.

[11] W.J. Luscher, K.J. Geelhood, and I.E. Porter, "Material property correlations: comparisons between FRAPCON-4.0, FRAPTRAN-2.0, and MATPRO. Technical Report PNNL-19417 Rev. 2," Pacific Northwest National Laboratory, 2015.

[12] D.R. Olander, "Fundamental Aspects of Nuclear Reactor Fuel Elements," Technical Information Center - Energy Research and Development Administration, 1976.

[13] C. M. Allison, G. A. Berna, R. Chambers, E. W. Coryell, K. L. Davis, D. L. Hagrman, D. T. Hagrman, N. L. Hampton, J. K. Hohorst, R. E. Mason, M. L. McComas, K. A. McNeil, R. L. Miller, C. S. Olsen, G. A. Reymann, and L. J. Siefken, "SCDAP/RELAP5/MOD3.1 code manual, volume IV: MATPRO-A library of materials properties for light-water-reactor accident analysis. Technical Report NUREG/CR-6150, EGG-2720," Idaho National Engineering Laboratory, 1993.

[14] Y. Rashid, R. Dunham, and R. Montgomery, "Fuel Analysis and Licensing Code: FALCON MOD01," Electric Power Research Institute, 2004.

[15] L. J. Siefken, E. W. Coryell, E. A. Harvego, and J. K. Hohorst, "SCDAP/RELAP5/MOD3.3 Code Manual: MATPRO-A Library of Materials Properties for Light-Water-Reactor Accident Analysis. NUREG/CR-6150, Vol.4, Rev.2," U.S. Nuclear Regulatory Commission, 2001.

[16] F. J. Erbacher, H. J. Neitzel, H. Rosinger, H. Schmidt, and K. Wiehr, "Burst criterion of Zircaloy fuel claddings in a loss-of-coolant accident," *American Society for Testing and Materials,* vol. 754, p. 271–283, 1982.

[17] Technical Report NUREG/CR-7024 Rev.1, "Material property correlations: comparisons between FRAPCON-3.5, FRAPTRAN-1.5, and MATPRO," Pacific Norhtwest National Laboratory, Richland, 2014.

[18] T.D. Blacker, S.J. Owen, M.L. Staten, W.R. Quadros, B. Hanks, B.W. Clark, R.J. Meyers, C. Ernst, K. Merkley, R. Morris, "CUBIT Geometry and Mesh Generation Toolkit 15.2 User Documentation," Sandia National Laboratory, Albuquerque, 2016.

[19] V. Di Marcello, A. Schubert, J. van de Laar, and P. Van Uffelen, "The TRANSURANUS Mechanical Model for Large Strain Analysis," *Nuclear Engineering and Design,* vol. 276, pp. 19-29, 2014.

[20] D. M. Perez, R. L. Williamson, S. R. Novascone, G. Pastore, J. Hales, B. W. Spencer, "Assessment of BISON: A nuclear fuel performance analysis code," Idaho Natl. Lab., Idaho Falls, 2013.

[21] R. L. Williamson, J. D. Hales, S. R. Novascone, G. Pastore, K. A. Gamble, B. W. Spencer, W. Jiang, S. A. Pitts, A. Casagranda, D. Schwen, A. X. Zabriskie, A. Toptan, R. Gardner, C. Matthews, W. Liu, and H. Chen, "BISON: A Flexible Code for Advanced Simulation of the Performance of Multiple Nuclear Fuel Forms," *Nuclear Technology,* vol. 207, pp. 954-980, 2021.

[22] C. J. Permann, D. R. Gaston, D. Andrs, R. W. Carlsen, F. Kong, A.D. Lindsay, J.M. Miller, J. W. Peterson, A. E. Slaughter, R. H. Stogner, "MOOSE: Enabling Massively Parallel Multiphysics Simulation," *ArXiv Prepr.,* vol. ArXiv1911.04488, 2019.

[23] B. S. Kirk, J. W. Perterson, R. H. Stogner, G. F. Carey, "LibMesh: A C++ Library for Parallel Adaptive Mesh Refinement/Coarsening Simulations," *Engineering with Computers ,* pp. 237-254, 2006.

[24] S. Abhyankar, J. Brown, E.M. Constantinescu, D. Ghosh, B.F. Smith, H. Zhang, "Petsc/ts: A modern scalable ode/dae solver library," *ArXiv Prepr,* p. ArXiv1806.01437, 2018.

[25] N. Capps, J. Hirschhorn, A. Wysocki, I. Greenquist, "Assessment of the Effect of Prototypic High-Burnup Operating Conditions of Fuel Fragmentation, Relocation, and Dispersal Susceptibility," ORNL, Oak Ridge, 2022.

[26] D. A. Powers and R. O. Meyer, "Cladding swelling and rupture models for LOCA analysis. Technical Report NUREG-0630," Nuclear Regulatory Commission, 1980.

[27] J. D. Hales, W. Jiang, A. Toptan, K. Gamble, "BISON TRISO Modeling Advancement and Validation to AGR-1 Data," Idaho National Laboratory, Idaho Falls, 2020 INL/EXT-20-59368.

[28] N. Capps, R. Sweet, B. Wirth, A. Nelson, and K. Terrani, "Development and demonstration of a methodology to evaluate high burnup fuel susceptibility to pulverization under a loss of coolant transient," *Nuclear Engineering and Design,* vol. 366, no. doi: 10.1016/j.nucengdes.2020.110744, pp. 1-29, 2020.